Suppression of precipitation bias on wind velocity from continuous-wave Doppler lidars

Liqin Jin, Jakob Mann, Nikolas Angelou, and Mikael Sjöholm

Department of Wind and Energy Systems, Technical University of Denmark, Frederiksborgvej 399, 4000 Roskilde, Denmark.

Correspondence: Liqin Jin (liqn@dtu.dk)

Abstract. In moderate to heavy precipitation, ~~rain droplets~~ raindrops may deteriorate Doppler lidars' accuracy for measuring the line-of-sight wind velocity because their projected velocity on the beam direction differs greatly from that of air. Therefore, we propose a method ~~of effectively filtering away~~ for effectively suppressing the adverse effects of rain on velocity estimation by sampling the Doppler spectra faster than the raindrops' beam transit time. By using a special averaging procedure, we can suppress the strong rain signal by sampling the spectrum at 3 kHz. ~~On~~ A proof-of-concept field measurement campaign was performed on a moderately rainy day with a maximum rain intensity of 4 mmh^{-1}, using three ground-based continuous-wave Doppler lidars ~~were used to conduct a field measurement campaign~~ at the Risø campus of the Technical University of Denmark. We demonstrate that the rain bias can effectively be removed by normalizing the noise-flattened 3-kHz-sampled Doppler spectra with their peak values before they are averaged down to 50 Hz prior to the determination of the speed. In comparison to the sonic anemometer measurements acquired at the same location, the wind velocity bias at 50 Hz (20 ms) temporal resolution is reduced from up to -1.58 ms^{-1} of the ~~conventional~~ original raw lidar data to -0.18 ms^{-1} of the normalized lidar data ~~. This significant~~ after suppressing strong rain signals. This reduction of the bias occurs at the minute with the highest amount of rain when the ~~measurement~~ focus distance of the lidar is 103.9 m with a corresponding probe length being 9.8 m. With the smallest probe length, 1.2 m, the rain-induced bias was only present at the period with the highest rain intensity and was also effectively eliminated with the procedure. Thus, the proposed method for reducing the impact of rain on continuous-wave Doppler lidar measurements of air velocity is promising, without requiring much computational effort.

1 Introduction

~~Accurate measurement of wind velocity is crucial for many applications in meteorology and wind energy. For example, precise~~ Precise determination of wind flow plays an important role in reducing loads on critical turbine components and power variations, correcting commonly used models for wind energy assessment, improving the performance of wind turbine controllers, and improving the prediction of the potential wind power extracted from the wind (Davoust et al., 2014; Jena and Rajendran, 2015; Li et al., 2018; Samadianfard et al., 2020; Guo et al., 2022). Besides, wind velocity estimation is also useful for understanding important phenomena, i.e., atmospheric boundary layer flows and wind turbulence (Van Ulden and Holtslag, 1985; Türk and Emeis, 2010; Debnath et al., 2017). Therefore, accurate measurements of wind velocity are ~~required, both in the industrial and academic areas~~ crucial for many applications in meteorology and wind energy.

There are several available instruments capable of measuring wind speed, wind direction, and turbulence in wind energy, each with advantages and disadvantages. ~~Compared with the in-situ anemometers, like cup or~~ In-situ cup and sonic anemometers installed on ~~the~~ meteorological masts (met masts) ~~, that provide point measurements albeit with an accurate measurement of the wind velocity~~ can provide only point measurements of wind velocity (Izumi and Barad, 1970). On the contrary, Doppler lidars ~~also have the potential to accurately measure the wind flow by precise measurements of the Doppler spectra~~ can accurately and remotely sense wind velocity by measuring Doppler spectra albeit with their limited ability in measuring turbulence due to probe-length averaging effects (Sathe and Mann, 2013). For more than a decade, Doppler lidars have been widely used as a more and more reliable, valuable, and active optical remote sensing instrument with easier and cost-effective deployment. They have been applied to estimate wind resource both onshore (Bingöl et al., 2009) and offshore (Sempreviva et al., 2008; Peña et al., 2009; Viselli et al., 2019; Elshafei et al., 2021), both by scanning lidars and profiling lidars (Mann et al., 2017; Menke et al., 2020; Gottschall et al., 2021) with good spatial and temporal resolutions (Henderson et al., 1991; Aoki et al., 2016).

Apart from the aforementioned, Doppler lidars have the potential of reducing loads on the turbine blade and tower through lidar prevision of the incoming gusts and flow (Bossanyi et al., 2014; Bos et al., 2016), and improving wind turbine control (Mikkelsen et al., 2013; Schlipf et al., 2015; Zhang and Yang, 2020). Doppler lidars can also be applied to study atmospheric turbulence along the span of a suspension bridge (Cheynet et al., 2016) and study the turbulent wind field in the near-wake region of a tree (Angelou et al., 2022). In order to improve the measurement accuracy by lidars, Wildmann et al. (2020) reduced the volume-averaging effect on the retrieval of the wind flow statistics with ground-based Doppler lidars (see also Sathe and Mann, 2013). Brinkmeyer (2015) suggested the low coherence Doppler lidar approach using a pseudo-random broadband laser source to obtain an effectively smaller sampling volume. It is self-evident that the precise determination of the wind velocity with Doppler lidars is paramount for many applications in wind energy.

~~Doppler lidars~~ Doppler lidars' measurements of wind velocity can be influenced by heavy rainfall because the projected ~~speed~~ velocity of raindrops on the propagation direction of the lidar beam will be different from the line-of-sight wind velocity. A synergy approach was proposed by ~~(Träumner et al., 2010)~~ Träumner et al. (2010), which combined radar and vertically scanning lidar measurements to estimate the vertical wind velocity and the raindrop size distribution during rain episodes. Later, by using a velocity-azimuth display (VAD) scanning technique, wind speed, and rainfall speed were simultaneously retrieved in ~~(Wei et al., 2019)~~ Wei et al. (2019), by fitting the two-peak spectrum with a two-component Gaussian model. The spectral peak close to $0\ \mathrm{ms^{-1}}$ is the Doppler signal of the vertical wind speed, which can be easily recognized in this scenario. Aoki et al. (2016) and Wei et al. (2021) proposed an iterative deconvolution method to retrieve raindrop size distribution during rain by using a vertically pointing coherent Doppler lidar.

However, for Doppler lidars which are not vertically pointing, the line-of-sight wind velocity is not close to zero and it is difficult to distinguish which part of the signal originated from ~~rain drops~~ raindrops or from air-following aerosols. Therefore, the purpose of the present study is to ~~experimentally investigate a method to filter away~~ provide a proof-of-concept experimental investigation of a method we propose to suppress the precipitation signal from the aerosol signals, in order to reduce the rain-induced bias on the velocity estimation.

A field measurement campaign was carried out at Risø where three coherent ~~ew~~ continuous-wave (CW) Doppler lidars (Mikkelsen et al., 2017) were deployed to point towards a common focus point very close to a mast-mounted sonic anemometer at 31 m height. Each lidar had different elevation angles, focus distances, and thus probe lengths. Therefore, it was possible to investigate the influence of these parameters on the performance of the post-processing method. The basic idea is to sample Doppler spectra rapidly, i.e. 3 kHz, which allows us to detect when a raindrop is in the beam~~and filter out those spectra~~. Measurements of a sonic anemometer are used as a reference to compare with the estimated line-of-sight wind velocity ~~of~~ by the three lidars, before and after ~~filtering away the rain component~~ suppressing rain Doppler signals in the Doppler spectra. The corresponding rain characteristics are retrieved from a ground-based disdrometer (Tilg et al., 2020) nearby the meteorological mast.

Section 2 introduces the field campaign and elaborately describes the instruments used. In Section 3, the measurement results of the sonic anemometers and the disdrometer are presented. The principle of Doppler spectral processing to retrieve the line-of-sight wind velocity as well as the method we propose to ~~filter away the rain signal~~ suppress strong rain signals are presented in detail in Section 4. Section 5 shows the comparison of 50 Hz and 1-minute wind velocity time series between the lidar and sonic anemometer measurements, with and without ~~filtering away~~ suppressing rain signals. The most important findings of our study are summarized in the Conclusion (Section 6).

2   Instrumentation

2.1   The WindScanner ~~lidar~~ system

In order to validate the method to reduce the influence of the precipitation on the estimated wind velocity, we conducted a field experiment at the Risø campus of the Technical University of Denmark (DTU), as shown in Fig. ~~??~~2. The surrounding terrain is flat and agricultural. The short-range WindScanner ~~lidar~~ system with three ~~ew~~ CW Doppler lidars (Fig. 1) which ~~is~~ are developed by DTU Wind and Energy Systems, was used to measure the wind field (Vasiljević et al., 2017; Mikkelsen et al., 2020). The three ~~WindScanners~~ lidars employ a dual-prism beam scanner, enabling them to orient the beam in any direction within ±61° of the adjustable center axis (Sjöholm et al., 2014; Mikkelsen et al., 2008). The direction of the line-of-sight of each lidar is steered by two prism motors and a focus motor controls the measurement location along the beam for these lidars. For this campaign, the sampling frequency of spectra is set to be 3 kHz. A central master computer is used to synchronize the short-range wind lidars to scan the same pattern in space simultaneously, however, all three ~~scanners~~ lidars are focused on one static point in this investigation. ~~Top view of the locations of three WindScanner lidars (indicated by the red points) near the Vestas V52 wind turbine © Google Maps.~~

The three ground-based ~~WindScanner~~ lidars were staring at a point 1 m north of a sonic anemometer (USA-1, METEK) which was located 31 m above the ground. The ~~scanner~~ lidar heads were covered with green rain barrels to avoid ~~rain droplets~~ raindrops covering the windows of the lidars (Fig. 1). The intention to use three ~~WindScanner~~ lidars is to investigate the influence of different probe lengths and different elevation angles on the performance of the method to ~~filter away~~ suppress rain signals. The full-width-at-half-maximum (FWHM) of the Lorentzian weighting function or the probe length can be approxi-
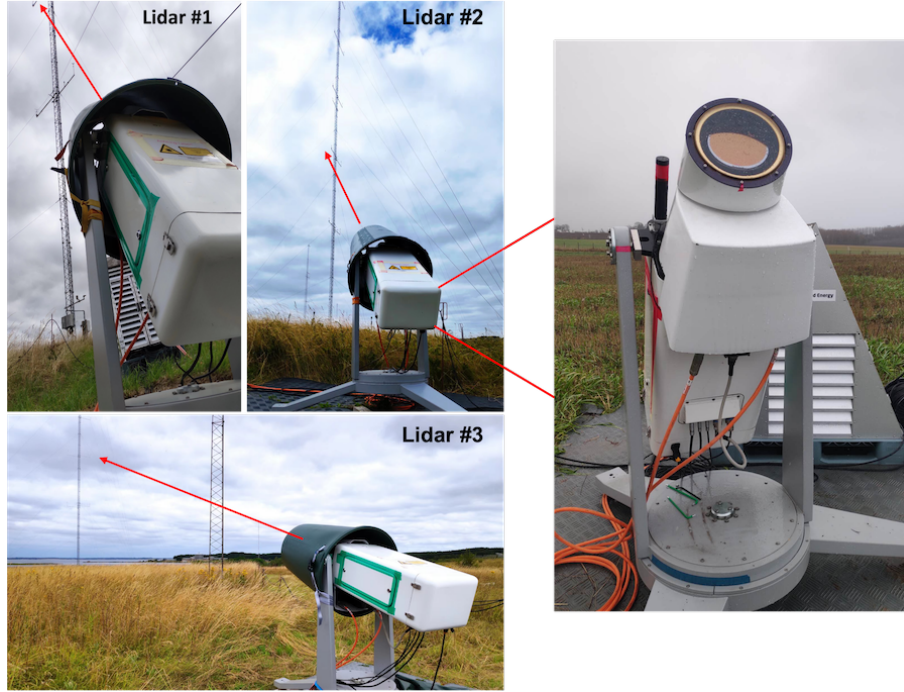
Figure 1. Three ~~WindScanner~~ CW lidars pointed at a common focus point close to a sonic anemometer on a met mast at DTU Risø campus.

mated as ~~,~~ (Sathe and Mann, 2013),

$$\text{FWHM} = 2 \cdot z_R = 2 \cdot \frac{\lambda \cdot R^2}{\pi r^2} \frac{\lambda \cdot R^2}{\pi a_0^2} \tag{1}$$

where z_R is the Rayleigh length, defined as the distance from the focus point to where the cross-sectional area of the laser beam is doubled (Angelou et al., 2012b), R is the distance from the lidar to where the beam is focused, λ is the laser wavelength, which is 1.565 μm, ~~r~~ a_0 is the e^{-2} intensity radius of the laser beam at the lidar telescope, which is about 33 mm. A list of the measurement parameters of the ~~WindScanner~~ three lidars is summarized in Table 1 and the three-dimensional view ~~, as well as the top view of the configuration of the three lidars,~~ of the three lidars' configuration is depicted in Fig. 2. ~~WindScanner unit~~ Lidar #1 is placed on a slope, therefore it has a relatively bigger elevation angle of about $58°$, but has the smallest probe length of 1.2 m, compared with ~~unit~~ lidar #2 and #3. The measurement period of the three ~~WindScanner~~ lidars is from 15:12 ~~(UTC+1)~~ to 23:29 (UTC+1) on September 27th, 2022. All times mentioned in the paper are UTC+1.

The backscattered light mixed and amplified by the local oscillator is sampled at a rate of 120 MHz and Doppler spectra containing 512 frequency bins are calculated ~~with a corresponding wind speed spectral resolution of about 0.183~~ by Fast Fourier Transform (FFT) with a frequency resolution of $(120\,\text{MHz})/512 = 234.4$ kHz. The wind speed resolution is calculated from this frequency resolution and the laser wavelength λ, yielding $(1.565\mu\text{m}/2)\cdot(234.4\,\text{kHz}) = 0.183$ ms^{-1}. In order to ~~be able to~~ determine the sign of ~~the~~ line-of-sight ~~velocity~~ velocities, the in-phase/quadrature-phase (IQ) detection method (Abari et al.,

4

Table 1. Summary of the measurement parameters of the ~~WindScanner~~ three CW lidars.

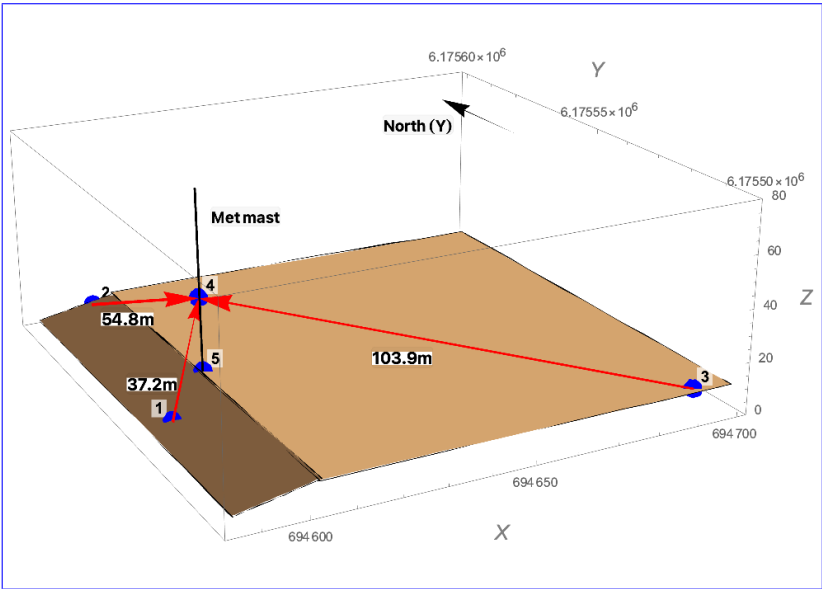| height	Elevation angle (°)	Rayleigh length z_R (m)	Line-of-sight focus distance R (m)	~~Angle to the North~~ Geographic beam
~~WindScanner~~ Lidar #1	57.9	0.6	37.2	~~222.6~~ 42.6
~~WindScanner~~ Lidar #2	34.6	1.4	54.8	~~-7.1~~ 172.9
~~WindScanner~~ Lidar #3	15.3	4.9	103.9	~~119.3~~ 299.3

Figure 2. ~~The 3D (a) and top view (b) of the configuration of the instruments~~ Experiment setup at DTU Risø campus in the three-dimensional view. ~~The blue~~ Blue points marked by 1, 2, and 3 are the three ~~WindScanner~~ CW Doppler lidars, focused at the common point 4 which is 1 m north of ~~a~~ the sonic anemometer at a height of 31 m above the ground. Point 5 is the base of the met mast. The black solid line indicates the met mast ~~in (a).The distances in (a) are the line-of-sight focus distances, while those in (b) are the projections on the horizontal plane.~~

2014) is employed, which mixes the received signal with two local oscillator ~~(LO)~~ signals phase shifted by 90° relative to each other. Subsequently, a block averaging of 78 spectra ~~takes place resulting~~ results in a final sampling period of $512 \cdot 78 /(120$ MHz$) = 0.33$ ms, corresponding to a spectrum rate of 3 kHz. Therefore, at every minute each ~~WindScanner~~ lidar will provide ~~a data file containing~~ 180000 spectra ~~in total. The reason for setting the spectral sampling frequency to 3 kHz is that the sampling period for a spectrum (0.33 ms) is less than the~~ . Additionally, Bartlett's method is used to obtain the power spectral density (PSD) of each spectrum (Press et al., 1988, Chap. 13), which is the square of the absolute value of the FFT of the detector's time series. The median method (Held and Mann, 2018) is employed to determine wind velocity.

115 The shortest beam transit time ~~(0.35 ms) of a typical raindrop. Here we found that the~~ can be determined based on large raindrops' maximum downfall speed of ~~raindrops is~~ 9 ms^{-1} from the disdrometer measurement (~~in~~ Fig. 6b) ~~and the calculated beam width is~~, the beam width (twice of the beam waist w_0), and the elevation angle of a lidar. For lidar #1 with a beam width of 1.12 mm and an elevation angle of 57.9°, the shortest beam transit time is 0.234 ms = 1.12/(9 · cos(57.9°)), while it is 0.362 ms = 3.14/(9 · cos(15.3°)) for lidar #3 with a beam width of 3.14 mm ~~when the focus distance is 103.9~~ and an

120 elevation angle of 15.3°. Most often, however, raindrops' transit time is longer than the aforementioned shortest time if their paths are away from the lidar focus and if they fall slower. In this study, it is reasonable to set the spectral sampling frequency to 3 ~~m. Consequently~~ kHz so that the sampling period for a spectrum (0.333 ms) is shorter than the beam transit of raindrops (see Jin et al., 2022, Fig. 5b). Therefore, the rare instances where a raindrop resides in the beam could be identified and suppressed based on the lidar measurements.

2.2 METEK sonic anemometer

125

The meteorological mast location is approximately 120 m northwest of the DTU V52 wind turbine and its base is 7.3 m above the sea surface (Fig. ~~??~~ 2). There are five sonic anemometers (USA-1, Metek) on booms facing north and five cup anemometers (~~Risø~~ P2546A from WindSensor) on booms facing south, placed at 18 m, 31 m, 44 m, 57 m, and 70 m above the terrain (Fig. 3). The sampling frequency of the sonic anemometers was 50 Hz. Furthermore, the mast is instrumented with a ~~wind vane~~ vector

130 wind vane (W200P from Kintech Engineering) at 41 m, and two ~~absolute temperature sensors~~ air temperature sensors (Pt 100, developed by DTU) mounted at 18 m and 70 m, respectively. In order to test the consistency of the mast wind measurements, the available sonic and cup observations at different heights are compared in the following section. The sonic anemometer at 31 m is used as a reference for further comparison with the radial wind velocity detected by the three ~~WindScanner~~ lidars.

In this step, it is also important to get accurate orientation of the sonic anemometer. For this purpose, the azimuth angle

135 of the boom is considered as the direction offset of the sonic anemometer relative to the North. Here the Leica Total Station (Fig. 3b) was used to scan the sonic anemometer at 31 m height, the boom at the same height, and the three ~~WindScanner lidars. Examples of the scanned results~~ lidars. The scanned results of the sonic anemometer at 31 m high are presented in Fig. ~~??~~ 3c and the azimuth angle of the boom to the north is 13.2° in the UTM32 zone and the tilt angle of the sonic to the vertical is 1.9°, which will be used to ~~compute~~ derive the unit vectors when projecting the reference sonic velocity onto the directions of

140 the three lidar beams. Consequently, the unit vectors of three lidars beams are [−0.36, −0.39, −0.85], [−0.10, +0.82, −0.57] and [+0.84, −0.47, −0.26], respectively. ~~Point clouds of (a) the sonic anemometer at the height of 31 m and (b) the head of the WindScanner unit #1, plotted in the local coordinate system of the Leica Total Station. The scans were used to derive the unit vectors of the three lidar beams.~~

It is evident from the sonic status information that wind velocity measurements by sonic anemometers can be affected by

145 raindrops. In those cases, the sonic anemometer would repeat the previous velocity value and the status would be "4". Thus, the linear interpolation method was used in this study to eliminate repeated velocities, which represented about 60% of the 50 Hz sonic data recorded at moderate-rain minutes.
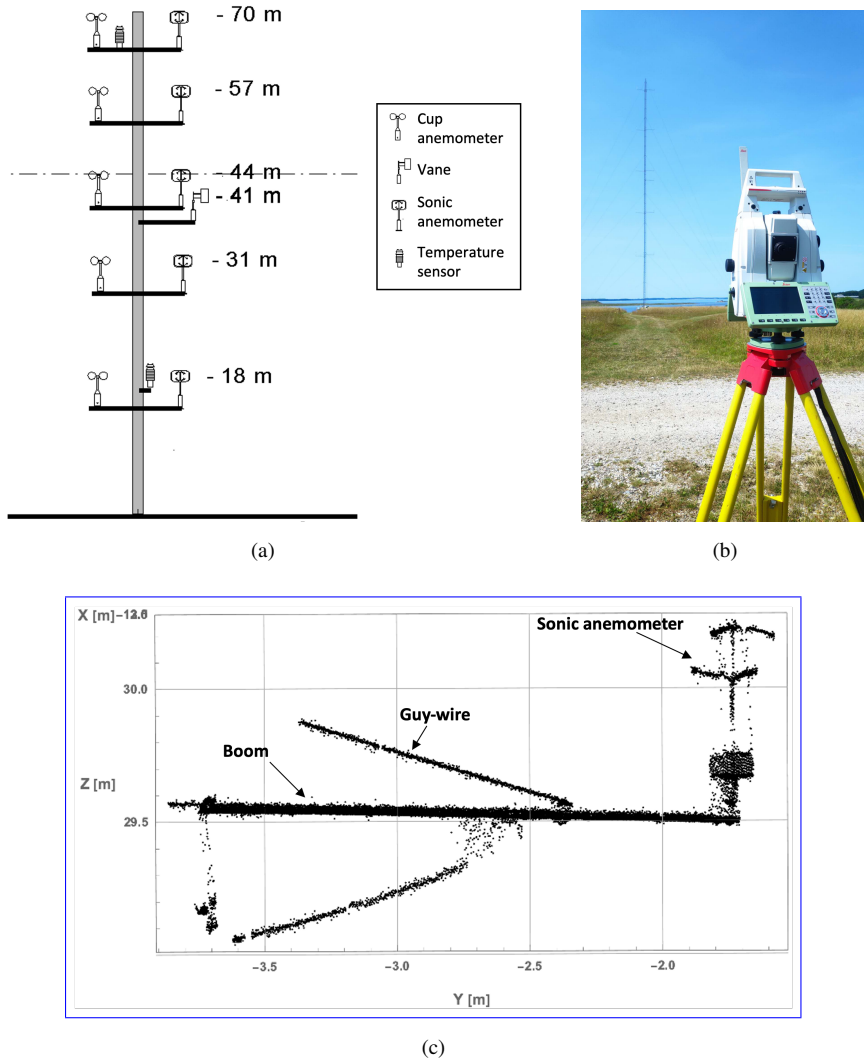
(a)

(b)

(c)

Figure 3. Orientation calibration of sonic anemometers on the met mast. **(a)** A sketch of the V52 meteorological mast with the instrumentation~~(a) and the~~. **(b)** Leica Total Station (Leica Geosystems, last access: 12 March 2023.)~~is used to scan~~. **(c)** Scanned cloud points of the sonic anemometer at the height of 31 m~~high (b)~~. The dashed line in **(a)** indicates the hub height of the DTU V52 wind turbine.

Figure 4. Thies Laser Precipitation Monitor(LPM) at DTU Risø campus.

2.3 Disdrometer measurements

The falling velocity and diameter of the ~~rain droplets~~ raindrops were measured by a laser optical disdrometer manufactured
by Thies (Laser Precipitation Monitor, LPM), with a transmitter head emitting a horizontal laser-light plane and a receiver
head detecting the emitted laser light (Fig. 4). When a ~~rain droplet~~ raindrop intersects the laser beam, it attenuates the power
of the transmitted laser light with a specific magnitude as a function of the falling velocity and the diameter. After the appli-
cation of a proprietary algorithm, the measured ~~droplets~~ raindrops are classified into specific velocity and diameter classes,
which are outputted with a temporal resolution of 1 minute. Here, ~~the droplet~~ raindrops' diameter is given as the equi-volume
sphere diameter (Angulo-Martínez et al., 2018). Some technical details of Thies LPM disdrometer are given in Table 2. This
disdrometer was about 20 m north of the met mast.

3 Sonic anemometer and disdrometer data

3.1 10-minute averaged sonic data

Before analyzing the sonic and lidar data, the sonic and cup wind speed as well as the sonic and vane wind direction at different
heights were compared. In Fig. 5 a and b we show that the 10-minute averaged wind speeds by sonic and cup anemometers
are in good agreement for all heights including the height of 31 m where the lidars were measuring. The slope of a linear
regression is 1.008 with a coefficient of determination R^2 equal to 0.997, which shows that wind speeds measured by the sonic

**Table 2.** Technical details of the Thies Laser Precipitation Monitor (LPM) (Clima, T, last access: 2 June 2023.).

	Thies LPM
Laser wavelength [nm]	786
Size of laser-light plane [mm^2]	4560
Number of diameter classes	22
Min ~~/max~~ of diameter classes [mm]	0.1875~~/ > 8~~
Number of velocity classes	20
Min/max of velocity classes [ms^{-1}]	0.1/15

anemometers agree well with that measured by cup anemometers (with only a 1% difference). The same conclusion can be drawn for the wind direction in Fig. ~~??~~5 c and d. Besides, the mean absolute difference of wind speed between the sonic and
165   cup anemometer at 31 m height is 0.11 ms^{-1} and that for wind direction between the sonic at 44 m and the vane at 41 m height is $1°$. However, for further comparison with the lidar data, the three unit vectors describing the direction of the line-of-sight are used to project the wind vector measured by the sonic anemometer onto the lidar's line-of-sight, as mentioned in Sect. 2.2. ~~Comparison of wind direction measured by sonic anemometers at five vertical heights (18, 31, 44, 57 and 70 m) and by wind vane at 41 m in (a) and the linear regression between sonic and vane wind direction as well as the fitted slope in (b). "W$_{dir}$"~~
170   ~~stands for the wind direction by the vane, while "S$_{dir}$" means measured by the sonic anemometer. The two red lines mark the comparison period of lidar and sonic data from 15:12 to 18:11.~~

   ~~Considering the scanners started to measure from~~ The experiment started at 15:12 ~~, the rain stopped after 19:00, and the wake influence of the DTU~~ (UTC+1) and stopped after three-hour measurements. This is because the measurement volumes came into the wake of the Vestas V52 wind turbine~~, three full hours of data were selected from~~. Whether a turbine wake affects
175   the measurements is unknown but we wanted to avoid this complication. From 15:12 to 18:11~~for the comparison, which is~~, marked by the two red vertical lines in Fig. 5~~and Fig. ??. From 15:12 to 18:11~~, the 10-minute mean wind speed ~~by~~ obtained from the sonic anemometer at ~~31m~~ 31 m is in the interval [2.02 ms^{-1}, 6.59 ms^{-1}], while the wind direction is in the interval [110.9°, 164.8°].

3.2   1-minute disdrometer data

180   The 1-minute averaged rain intensity from 15:00 to 19:30 ~~measured by~~ (UTC+1) measured by the Thies disdrometer is shown in Fig. 6a. It started to rain at 15:15, reached the highest precipitation rate of about 4 mmh^{-1} at 15:48, and stopped after 19:00. ~~The Met Office defines moderate rain~~ Moderate rain is defined as a precipitation rate between ~~2.5~~2.6 mm and 7.6 mm per hour (Glossary of Meteorology (June 2000), last access: 21 June 2023.). The selected comparison period from 15:12 to 18:11

9
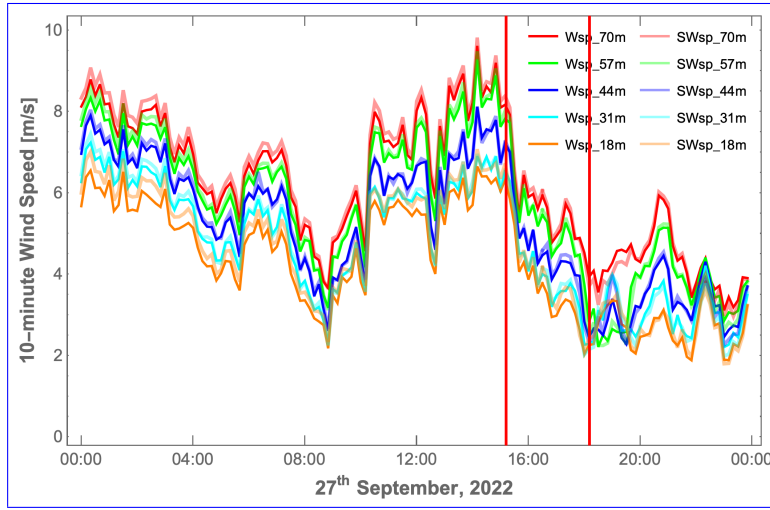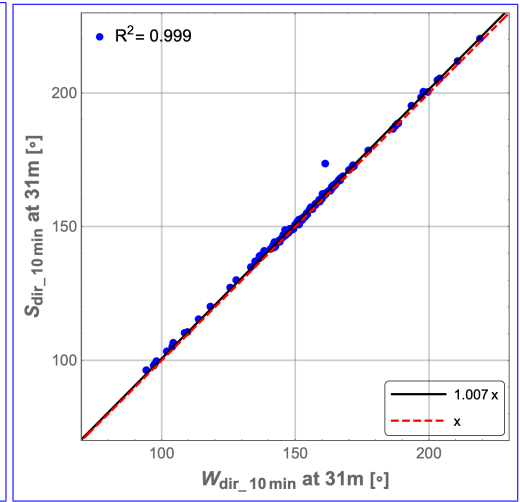
(a)
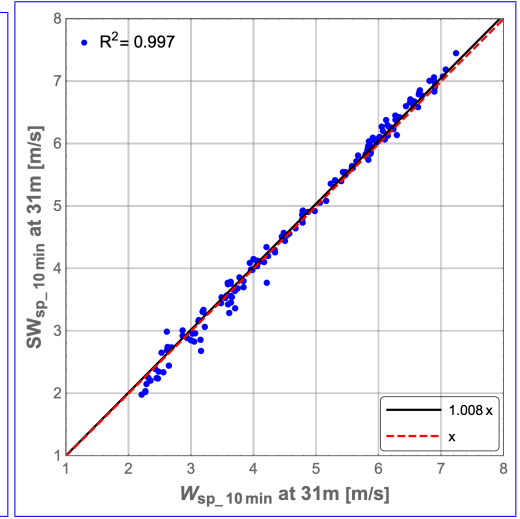
(b)
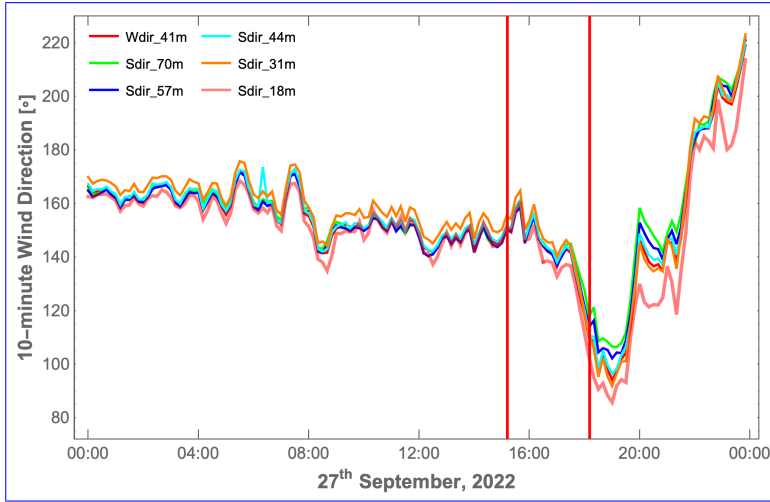
(c)

(d)

Figure 5. Comparison of 10-minute wind speed measured by measurements with the wind vane, sonic and cup anemometers at five several vertical heights. **(a)** 10-minute wind speed by sonic (18, 31, 44, 57 and 70 mSW$_{sp}$) in **(a)** and the linear regression between sonic and cup wind speed as well as the fitted slope in **(b)**. "(W$_{sp}$" stands for the) anemometers. **(b)** 10-minute wind speed direction by cup anemometer, while "SW$_{sp}$" means measured by the sonic anemometeranemometers (S$_{dir}$) and the wind vane (W$_{dir}$). **(c)** and **(d)** Linear regression of 10-minute wind speed and direction. The two red lines mark the comparison period of lidar and sonic data from 15:12 to 18:11.11 (UTC+1).
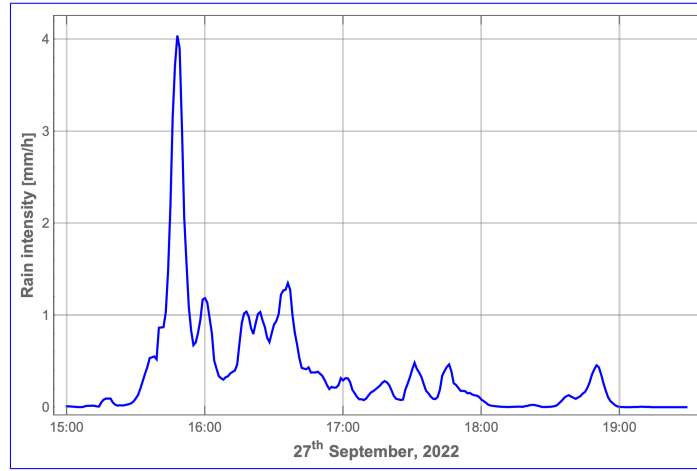
(a)
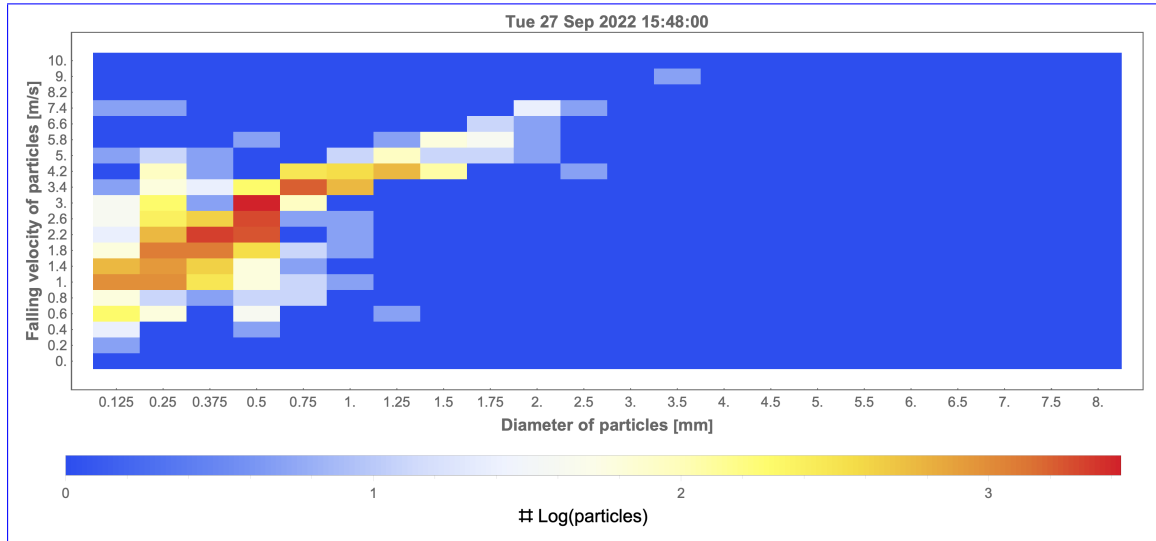
(b)

Figure 6. Rain ~~intensity~~ event from 15:00 to 19:30 (UTC+1) on September 27th, 2022 ~~based on~~ measured by the ~~measurement from the~~ Thies Laser Precipitation Monitor disdrometer. **(a)** ~~and the color-coded boxes represent the distribution~~ 1-minute Rain intensity. **(b)** Distribution of the number of measurements with specific vertical falling speeds and mass-weighted mean diameters at ~~one~~ the minute (15:48) with the highest rain intensity ~~(b)~~ (color coded).

includes no-rain, light-rain (the precipitation rate is smaller than 2.5 mmh^{-1}), and moderate-rain minutes, which enables the
185 investigation of the performance of the method we propose to ~~filter away~~ suppress rain signals during precipitation levels.
During the highest rain intensity period, most of the raindrops have mass-weighted mean diameters smaller than 2 mm and the
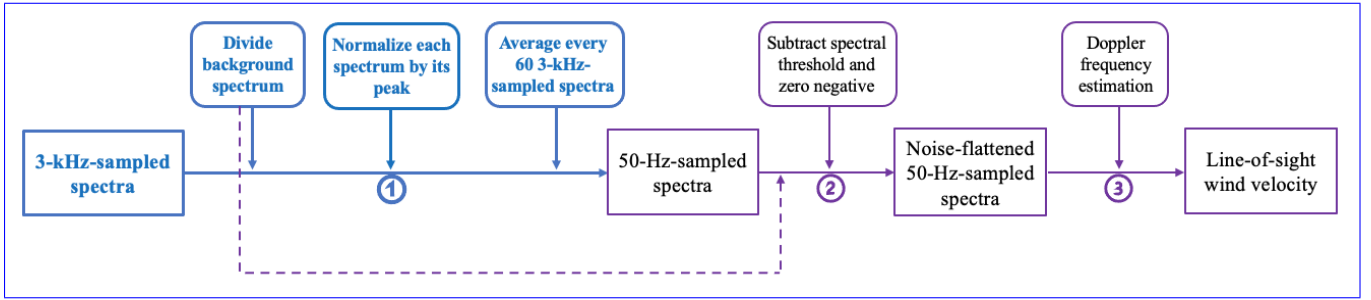falling velocity smaller than 6 ms^{-1} as shown in Fig. 6b.

Figure 7. Processing block diagram of the rain-suppressing normalization method (the solid lines from ① to ③) to estimate wind velocity based on 3-kHz-sampled Doppler spectra. Doppler spectra at lower frequencies that do not resolve individual raindrops (like 50 Hz) are processed according to the purple path including the dashed purple line, ②, and ③.

4 Suppression method of the ~~rain-bias~~rain bias

4.1 Lidar data processing

190 ~~The raw lidar data without filtering away the rain signal (marked by "Raw") is processed by following the conventional procedure to retrieve a line-of-sight wind velocity. Firstly, every raw spectrum (the blue curve~~ Doppler spectra are usually averaged to lower frequencies, ranging from 50 Hz to a few hundred Hertz. A 50-Hz-sampled spectrum can be processed by the following steps (the purple path marked by ② and ③ in Fig. ~~8a)is divided with~~ 7 along with the dashed purple line): the spectrum is divided by the background spectrum ~~(the red curve in Fig. 8a) to flatten the noisefloor. The background spectrum is~~

195 ~~calculated as the median power spectral density per frequency of 180000 Doppler spectra, acquired during a one-minute period. After that, we choose the smaller background for any pair of frequencies $(-f, f)$, which provides the true background even if the wind velocity is constant over the minute. However, if the wind velocity is around zero, this procedure does not work. Therefore, in the case of lidar #1 where the~~ and subtracted by its spectral threshold to flatten background noise. Consequently, the line-of-sight velocity ~~fluctuates around zero, a background spectrum is calculated for a period where the line-of-sight speed~~

200 ~~is away from zero.~~

~~Secondly, the 3 kHz spectra are averaged down to~~ is retrieved based on this noise-flattened 50 ~~Hz to ease comparison with the sonic anemometer. Then, the spectral threshold (the red line in Fig. 8c) of each spectrum is calculated based on the mean value (μ) plus multiple numbers of the standard deviation (σ) of the power spectral density over a wind-free Doppler frequency range. The final 50~~ Hz spectrum ~~used to estimate the line-of-sight wind velocity is obtained from Fig. 8c, by subtracting the spectral~~

205 ~~threshold and zeroing the negative values. Three different methods can typically be used to find the line-of-sight velocity from the spectrum: the maximum method, the centroid method, and the median method (see comparison made by Held and Mann, 2018) . The median method is employed in this investigation because it is characterized by the least biases in the case of weak signals (Angelou et al., 2012a).~~ after applying Doppler frequency estimation methods (Peña et al., 2015, Chap. 5).

However, from a random 3 kHz spectrum acquired during a ~~1-minute period~~ minute (15:48, UTC+1) with moderate-rain precipitation, it is obvious that sometimes the spectrum has a very high, narrow peak as shown in Fig. 8b. This is caused by a raindrop falling through the beam, the intensity of which should be compared to the ones of the more commonly occurring spectra where the Doppler signal is caused by the aerosols (Fig. 8a). Here the width of the Doppler spectrum in Fig. 8a is relatively wider because the aerosols within the measurement volume of the lidar have slightly different velocities and the peak value is much lower. In contrast, the spectrum caused by the raindrop is very narrow because of the single velocity of the drop. From the histogram, (Fig. 8d) of the maximum values of the spectra obtained during this moderate-rain minute, the very high back-scattering events marked by the red circle are the large raindrops passing through the center line of the laser beam close to the beam waist. These could potentially cause a bias between the radial wind velocity measured by the lidar and by the sonic.

Therefore, based on the above observations, ~~a method is proposed~~ we propose the rain-suppressing normalization method to reduce the influence of rain on ~~the averaged Doppler spectra. This is done by normalizing each individual noise-flattened spectrum with its peak value and then downsampling the 3 kHz spectra~~ wind velocity estimation. The detailed process is indicated by the solid lines and marked by ① to ③ in Fig. 7, which is:

① every 3-kHz-sampled Doppler spectrum without suppressing rain signal (blue curve marked by "Raw" in Fig. 8a) is divided with the background spectrum (red curve in Fig. 8a) to flatten the noise floor. Then, the noise-flattened 3-kHz-sampled spectra are normalized by their own peak value. Subsequently, every 60 normalized spectra are averaged down to 50 Hz ~~. The subsequent steps would be the same as~~ to achieve a better signal-to-noise ratio (Branlard et al., 2013) and ease the comparison with the sonic anemometer;

② a spectral threshold (black line in Fig. 8c) is subtracted from every 50 Hz spectrum and negative values are zeroed. The spectral threshold is calculated based on the mean value (μ) plus multiple numbers of the standard deviation (σ) of the power spectral density over a wind-signal-free Doppler frequency range;

③ the median method is used to determine line-of-sight velocity from the final 50 Hz spectra (Fig. 8c), as it has the least biases for weak signals (Angelou et al., 2012a) in comparison to the ~~aforementioned process to deal with the original raw spectra, i. e. , subtract the spectral threshold, replace negative values with zero , and lastly apply the median velocity estimation method to calculate wind velocity.~~ maximum and centroid methods (Held and Mann, 2018).

In the first step, the background spectrum is calculated as the median power spectral density per frequency of 180000 Doppler spectra, acquired during one minute. After that, we choose the smaller background for any pair of frequencies $(-f, f)$, which provides the true background noise even if the wind velocity is constant over the minute. However, this procedure will not work if the wind velocity is around zero, since the wind Doppler signal would be present on both sides of the zero frequency bin. Then a real, atmospheric Doppler signal would be included in the background spectrum rather than the real background noise. Therefore, in the case of lidar #1 where the line-of-sight velocity fluctuates around zero (the vertical line at frequency bin 257 corresponding to the zero-Doppler shift in Fig. 8), a background spectrum is calculated for a period where the line-of-sight speed is away from zero.
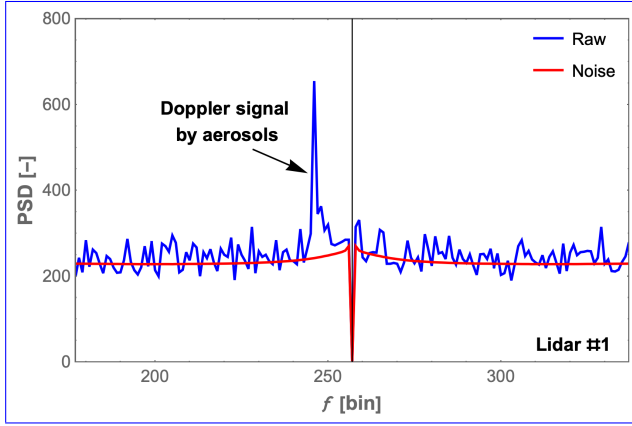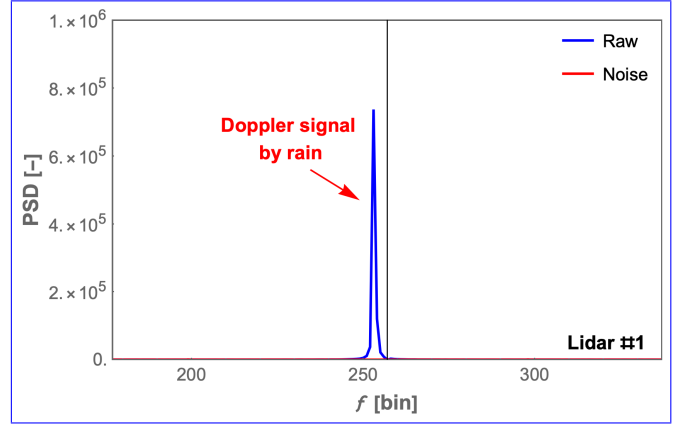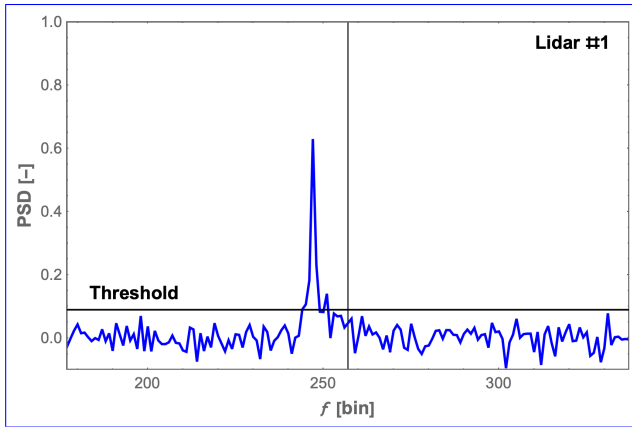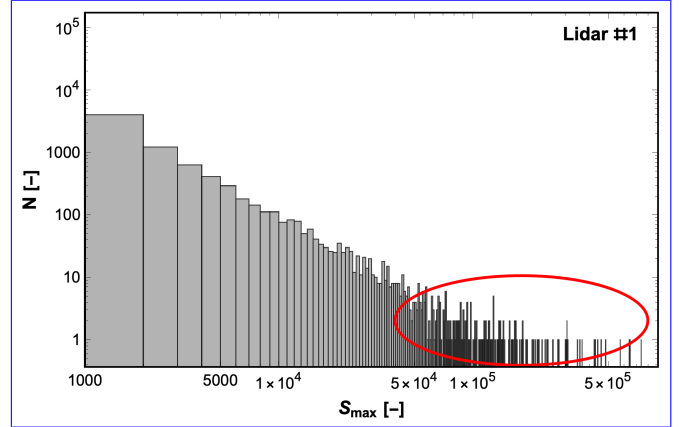
Figure 8. Examples of ~~a normal~~ representative Doppler ~~spectrum containing wind signal (a) and a spectrum containing rain signal (b)~~ spectra measured at ~~one~~ the moderate-rain minute (15:48, UTC+1) with the highest rain intensity. **(a)** A 3-kHz-sampled spectrum containing only wind signal (blue) and the mean background spectrum (red). **(b)** A 3-kHz-sampled spectrum containing rain signal (blue) and the mean background spectrum (red). **(c)** ~~is one example of a 50-Hz~~ A noise-flattened 50-Hz-sampled spectrum and ~~the corresponding~~ its spectral threshold. **(d)** ~~shows the histogram~~ Histogram of the maximum ~~power~~ spectral ~~density values~~ energy S_{max} of 180000 raw spectra over the duration of the same minute ~~. The red curve in (a) and (b) is the mean background spectrum of this one minute. Toward the right of (d),~~ with a red circle ~~marks~~ marking the strongest rain signals. The solid black line stands for the zero-Doppler shift at frequency bin 257.

After ~~flattening the noise floor~~obtaining 50 Hz spectra in the third step, it is vital to determine a correct spectral threshold to define the signal caused by the wind in a Doppler spectrum. This is because a too-high spectral threshold would result in the unexpected removal of the useful Doppler signal and cause false 0 ms^{-1} wind velocity, while a too-low spectral threshold would leave a lot of noise in the spectrum, deteriorating the accuracy of the wind velocity estimation. As concluded in ~~(Angelou et al., 2012a)~~Angelou et al. (2012a), the optimum number of standard deviations ~~for defining~~ to define the threshold is not the same for different data sets~~and a~~. After calculating velocity difference with sonic data over a short period of time, a number of 2.5 has been ~~used~~ chosen for the three lidars in this ~~investigation~~study.

4.2 Lidar spectra with and without ~~rain-removal~~ rain-suppressing normalization

It is important to point out that during the measurement time from 15:12 to 18:11 ~~, WindScanner~~ (UTC+1), lidar #2 was facing the wind almost all the time and we speculate that rainwater was covering the entrance window of the lidar telescope, despite our attempt to shield the window with a green rain barrel (Fig. 1). The water caused a very weak Doppler spectrum even at the minute with the highest rain intensity. Therefore, for further analysis and comparison, only the measurement data by lidar #1 and #3 are used.

It is worth noting that the wind direction at the minute with the highest rain intensity (15:48, UTC+1) is from 160° by the 10-minute averaged sonic data~~and the orientations of the two scanners are 222.6° and 119.3° to the north~~, and the two lidars' geographic beam directions are 42.6° and 299.3° (Fig. 2~~b), revealing that at this minute the wind moves away from the laser beams of both lidars, causing red Doppler shift~~). Therefore, the wind is moving away from both lidars' laser beams at this minute, causing negative line-of-sight velocity. Consequently, the projection of the resultant velocity of raindrops, in the measuring configuration used here, is smaller than that of the horizontal wind speed in the beam direction. In Fig. 9, it is very obvious that after normalization by the spectral peak, the narrow Doppler signal caused by the raindrops (~~marked by the red arrow~~red arrows) is effectively suppressed and the bias between the reference sonic wind velocity and that of the lidars is reduced as can also be seen in Table 3, for example, from -1.56 to -0.18 ms^{-1} at 50 Hz for lidar #3. This indicates that normalization by the spectral peak value can help to reduce the influence of the ~~rain droplets~~ raindrops since the narrow peak closer to the center zero frequency (the solid black line at frequency bin 257) is strongly suppressed.

~~Therefore, based on the promising results about the effective suppression of the rain Doppler signals at one moderate-rain minute (15:48), in the following section~~ In the section below, we compare the radial wind velocity detected by ~~WindScanner~~ lidars and the sonic anemometer at 31 m height in ~~details~~detail in light of the promising results about the effective suppression of rain Doppler signals at one moderate-rain minute (15:48, UTC+1). The outcomes are elaborated to verify this rain-suppressing normalization method under no-rain, light-rain, and moderate-rain conditions.
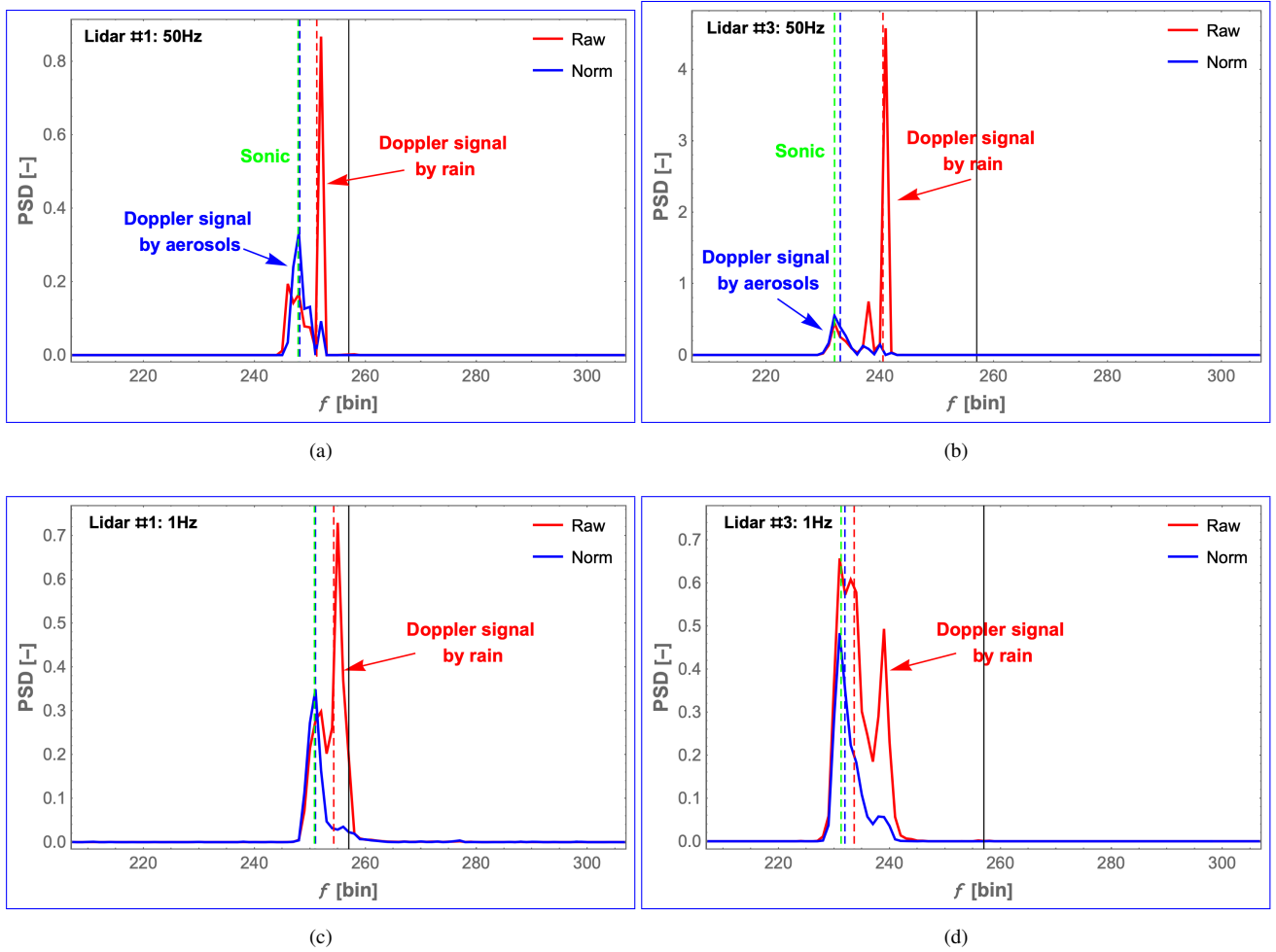
Figure 9. Comparison of ~~50 Hz ((a), (b)) and 1 Hz ((c), (d))~~ Doppler spectra containing both wind and rain ~~signal for WindScanner lidar #1 and #3 at one moderate-rain minute (15:48). The red solid curves represent the standard-average spectra without filtering away the rain~~ Doppler signals, with (marked by "~~Raw~~Norm" ~~), while the blues are after rain-suppressing~~ short for normalization~~by the spectral peak to filter away the rain signals~~) and without (marked by "~~Norm~~Raw"~~short~~) suppressing rain signals for ~~normalization~~two lidars at the moderate-rain minute (15:48, UTC+1). **(a)** and **(b)** 50-Hz-sampled spectra for lidar #1 and #3. **(c)** and **(d)** 1-Hz-sampled spectra for lidar #1 and #3. The red and blue dashed lines represent ~~for~~ the median frequency bin of the ~~standard averaged~~ raw and the ~~rain-suppressing averaged~~ normalized Doppler spectra, which are used to derive line-of-sight wind velocity. The green dashed line indicates the sonic wind velocity ~~. The~~ and the solid black line stands for the ~~zero~~ zero-Doppler shift at frequency bin 257.

Table 3. The estimated wind velocity by lidar data with (V_{norm}) and without (V_{raw}) normalization, and by the sonic anemometer (V_{sonic}) from 50 Hz and 1 Hz spectra at ~~one~~ the moderate-rain minute (15:48, UTC+1).

	V_{sonic} (ms^{-1})	V_{raw} (ms^{-1})	V_{norm} (ms^{-1})
50 Hz of #1	-1.67	-1.06	-1.62
50 Hz of #3	-4.58	-3.02	-4.40
1 Hz of #1	-1.14	-0.50	-1.10
1 Hz of #3	-4.72	-4.29	-4.59

5 Comparison between lidar and sonic wind velocity

5.1 50Hz wind velocity comparison

The reference 50 Hz sonic data at 31 m height was synchronized with the lidar measurements before the comparison. ~~Based on the sonic status information, we interpolated repeated sonic wind velocity measurements, that occurred due to the influence of the raindrops.~~ In Fig. 10~~a, c, e and Fig. ??a, c, e,~~, the 50 Hz radial wind velocity time series of the normalized lidar data (~~the~~ blue curves) matches well with the synchronized sonic data (~~the~~ green curves) at the no-rain, light-rain ($I_{rain} = 1$ mmh^{-1}) and moderate-rain ($I_{rain} = 4$ mmh^{-1}) minutes. It is very clear that the fluctuation of the wind velocity caused by the raindrops is effectively suppressed, especially during the moderate-rain period for lidar #1 with a shorter focus distance 37.2 m in Fig. 10e, or during the rainy period for lidar #3 with a longer focus distance 103.9 m in Fig. ~~??c and e~~10d and f. This can also be found from R^2 ~~of the scatter plots in Fig. 10 and ??~~values, indicating less dispersion of the lidar wind velocity after rain-suppressing normalization.

Furthermore, Tables 4 and 5 compare the minute-averaged radial wind velocity of the three data sets (sonic, ~~standard-averaged lidar data~~ original raw lidar data without rain-suppressing normalization, and rain-suppressing normalized lidar data) as well as the bias between the sonic and lidar estimations. In the case of small probe lengths (lidar #1), only at the moderate-rain minute, the bias is effectively reduced from -0.15 to -0.04 ms^{-1} after normalization, whereas the bias is almost the same at the no-rain and light-rain minutes. However, precise wind velocity is obtained after normalization of lidar #3 data in the presence of light rain and moderate rain, with the bias correspondingly reduced from -0.21 to -0.01 ms^{-1} and from -0.33 to -0.08 ms^{-1}. In light of this, it follows that when the probe length is small and it rains more heavily than lightly, rain-suppressing normalization by the spectral peak value can ~~filter out~~ suppress the rain signals effectively. However, when the probe length is larger (up to 10 m) with a broader Lorentzian weighting function, normalization performs very well when rain falls (whether light or heavy) because of the sensitivity of the lidar to rain signals. ~~Comparison of 50 Hz radial wind velocity (the left column) and the scatter plot (the right column) of the sonic data (the green curves), the raw (the red curves and dots),~~
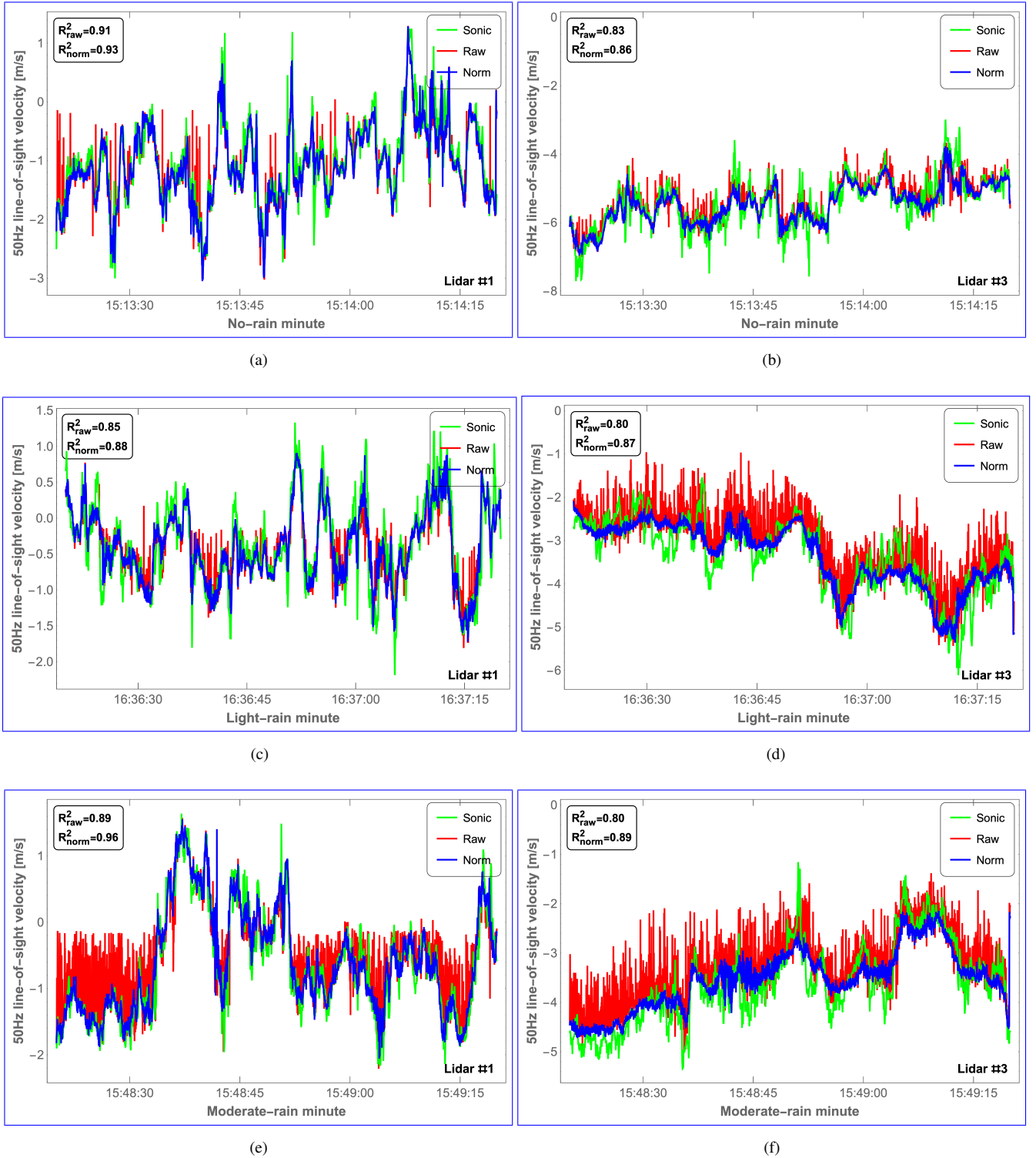
Figure 10. Comparison of 50 Hz radial wind ~~velocity (the left column) and the scatter plot (the right column) of the~~ <u>measurements by</u> sonic ~~data (the~~ green~~curves)~~ ~~, the raw (the red curves~~ and ~~dots), and the normalized~~ lidar ~~data (the blue curves~~ <u>red</u> and ~~dots~~<u>blue</u>) ~~for WindScanner~~ ~~lidar #1~~ at the no-rain, light-rain<u>,</u> and moderate-rain minutes from top to bottom. **<u>(a), (c), and (e)</u>** <u>Lidar #1 (probe length of 1.2 m).</u> **<u>(b), (d),</u>** <u>and **(f)** lidar #3 (probe length of 9.8 m).</u> The ~~solid black line indicates y=x~~<u>raw and normalized lidar data are marked in red and blue.</u>

18

Table 4. 1-minute averaged wind velocity based on 50 Hz data and the corresponding bias between the sonic anemometer and ~~WindScanner~~ lidar #1 (probe length of 1.2 m) at three minutes, with (norm) and without (raw) normalization. Rain intensity at the light-rain and moderate-rain minutes are 1 mmh^{-1} and 4 mmh^{-1}.

	V_{sonic} (ms^{-1})	V_{raw} (ms^{-1})	$V_{sonic} - V_{raw}$ (ms^{-1})	V_{norm} (ms^{-1})	$V_{sonic} - V_{norm}$ (ms^{-1})
No-rain minute 15:13:20+1min	-1.01	-1.07	0.06	-1.08	0.07
Light-rain minute 16:36:20+1min	-0.38	~~-0.391~~ -0.39	~~0.11~~ 0.01	~~-0.394~~ -0.39	~~0.14~~ 0.01
Moderate-rain minute 15:48:20+1min	-0.64	-0.49	-0.15	-0.60	-0.04

Table 5. 1-minute averaged wind velocity based on 50 Hz data and the corresponding bias between the sonic anemometer and ~~WindScanner~~ lidar #3 (probe length of 9.8 m) at three minutes, with (norm) and without (raw) normalization. Rain intensity at the light-rain and moderate-rain minutes are 1 mmh^{-1} and 4 mmh^{-1}.

	V_{sonic} (ms^{-1})	V_{raw} (ms^{-1})	$V_{sonic} - V_{raw}$ (ms^{-1})	V_{norm} (ms^{-1})	$V_{sonic} - V_{norm}$ (ms^{-1})
No-rain minute 15:13:20+1min	-5.42	-5.41	-0.01	-5.45	0.03
Light-rain minute 16:36:20+1min	-3.37	-3.16	-0.21	-3.36	-0.01
Moderate-rain minute 15:48:20+1min	-3.62	-3.29	-0.33	-3.54	-0.08

~~and the normalized lidar data (the blue curves and dots) for WindScanner lidar #3 at the no-rain, light-rain and moderate-rain minutes from top to bottom. The solid black line indicates y=x.~~

295   In addition, the same conclusions can be drawn by comparing the probability density function (PDF) calculated for the radial wind velocity estimated based on the 1-minute averaged lidar spectra and the 50 Hz sonic data at three minutes, as shown in Fig. 11. The improvement by normalization for lidar #1 with a smaller probe length is observed only during the moderate rain period (Fig. 11e), as the calculated integral of the absolute difference of the PDF is reduced from 3.04 to 1.08 in Fig. 12. For lidar #3 with a larger probe length, normalization performs very well not only at the moderate-rain minute in Fig. 11f but also

300   at the light-rain minute in Fig. 11d with the reduction of the integral of the absolute difference of the PDF from 1.68 to 0.57. In the comparison of the integral ~~value~~ of the absolute difference of the PDF alone, normalization performs very well during rain periods when the probe length is large, or during moderate rain when the probe length is smaller, which is consistent with the conclusions discussed above.

~~When~~ At every minute, R^2 of lidar #3 is smaller than that of lidar #1 when comparing R^2 of the original raw lidar data ~~at~~

305   ~~the same minute between lidar #1~~ in Fig. 10~~b, d, f, and lidar #3 in Fig. ??b, d, f, it is easy to find that R^2~~. We are uncertain
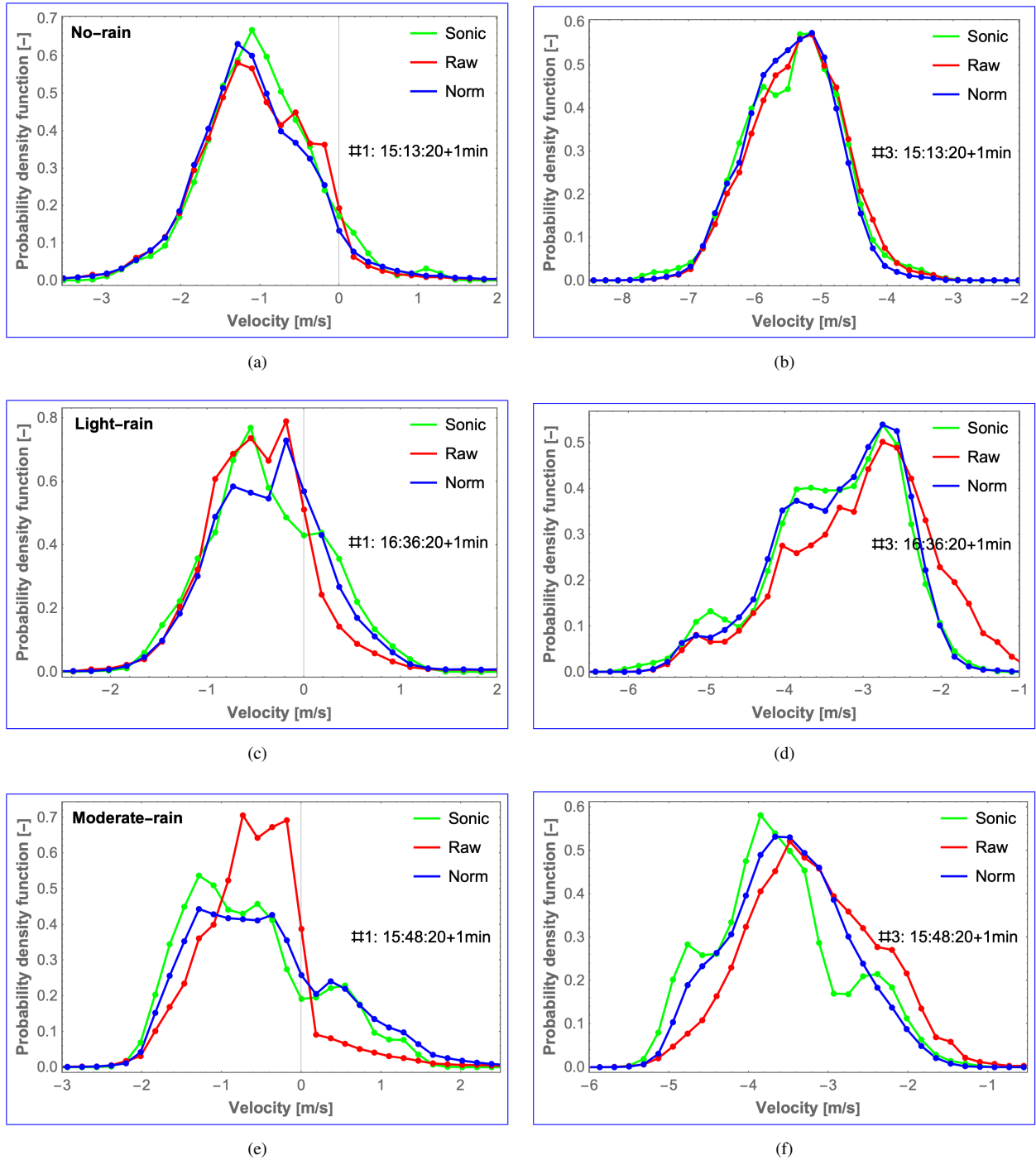
Figure 11. ~~Comparison of the probability~~ <u>Probability</u> density function (PDF) of ~~the estimated~~ radial wind velocity by 1-minute ~~averaged spectra of the raw~~ lidar ~~data without normalization~~ <u>spectra</u> (~~the~~ red ~~curves)~~ and ~~the normalized lidar data (the~~ blue<u>curves</u>) ~~as well as the histogram of the 50 Hz~~ <u>and 1-minute</u> sonic data <u>(green)</u> at the no-rain (top row), light-rain (second row)<u>,</u> and moderate-rain (bottom row) ~~for WindScanner lidar #1 (~~<u>minutes.</u> **(a)**, **(c)**<u>,</u> and **(e)** ~~) and #3 (~~<u>Lidar #1.</u> **(b)**, **(d)**<u>,</u> and **(f)** ~~)~~<u>Lidar #3. The raw and normalized lidar data are marked in red and blue.</u>
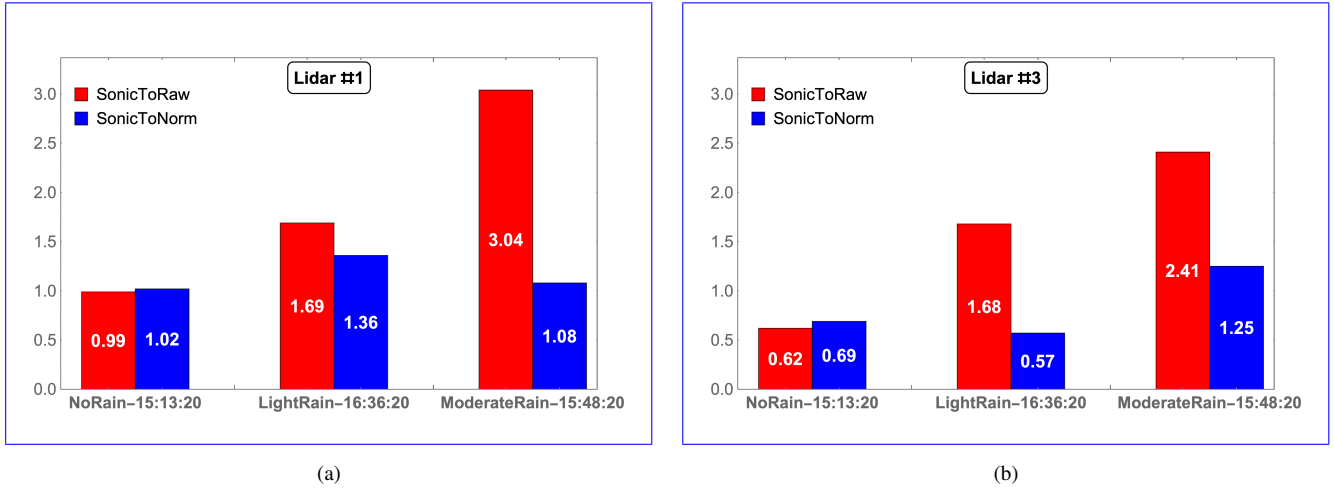
Figure 12. Comparison of the integral value of the ~~PDF's~~ absolute difference ~~of the PDF~~ between the sonic and the lidar data ~~sets~~ with (~~the right column~~SonicToNorm) and without (~~the left column~~SonicToRaw) rain-suppressing normalization at no-rain, light-rain ($I_{rain} = 1$ mmh^{-1}), and moderate-rain ~~minutes of the two WindScanners based on the probability density function (PDF~~$I_{rain} = 4$ mmh^{-1}) ~~in Fig~~minutes. ~~11~~(**a**) Lidar #1. (**b**) Lidar #3.

about why rain seems to deteriorate the wind signal of lidar #3 ~~is smaller~~ more than that of lidar #1~~at every minute. This is because the larger probe length of lidar~~. It could have to do with the larger sample volume of #3 ~~, 9.8 m, dominantly influences the variation of the estimated wind velocity, even though the elevation angle of lidar #1 (57.9°) is much larger than that of lidar #3 (15.3°). Besides, due to the very big elevation angle of lidar #1, it would be easier to have a smaller projection of the horizontal wind speed or of the resultant raindrop velocity on the line-of-sight beam direction, even zero projection in some cases, as depicted in the scatter plots in Fig. 10b, d and~~ for the different elevation angles, but it could also have to do with a different amount of raindrops on the entrance windows of the telescope. The understanding of these sensitivities awaits more experimentation.

5.2 1-minute wind velocity comparison

The bias between the 1-minute sonic wind velocity and the lidar wind velocity, along with the rain intensity, are presented in Fig. 13. From the figure, we can draw similar conclusions as described previously. In the case of the lidar #1 with a smaller probe length in Fig. 13a, after normalization with the spectral peak, the large bias of the red curve around the rain intensity peak is effectively reduced from -0.15 to -0.03 ms^{-1}. This is a result of ~~filtering away~~ suppressing the low and negative velocities caused by raindrops. For other minutes, the estimated wind velocity after normalization is almost the same as the raw data, which ~~is in line~~ aligns with the conclusions from 50 Hz data in Sect. 5.1.

For lidar #3, the improvement of wind velocity estimation by normalization is highly effective as presented in Fig. 13b, from when it started to rain at 15:29 until 16:~~48. Afterwards~~48 (UTC+1). Afterward, at some minutes, the wind velocity time
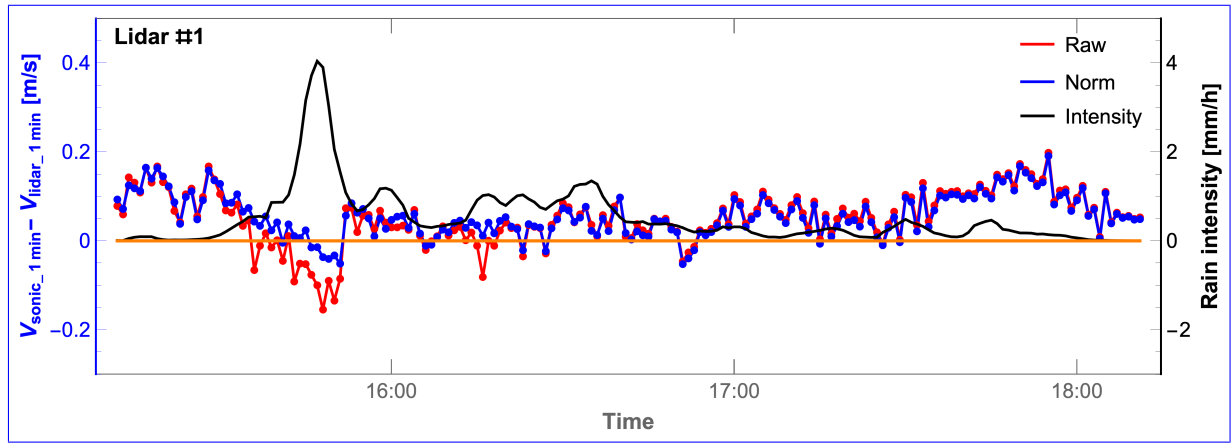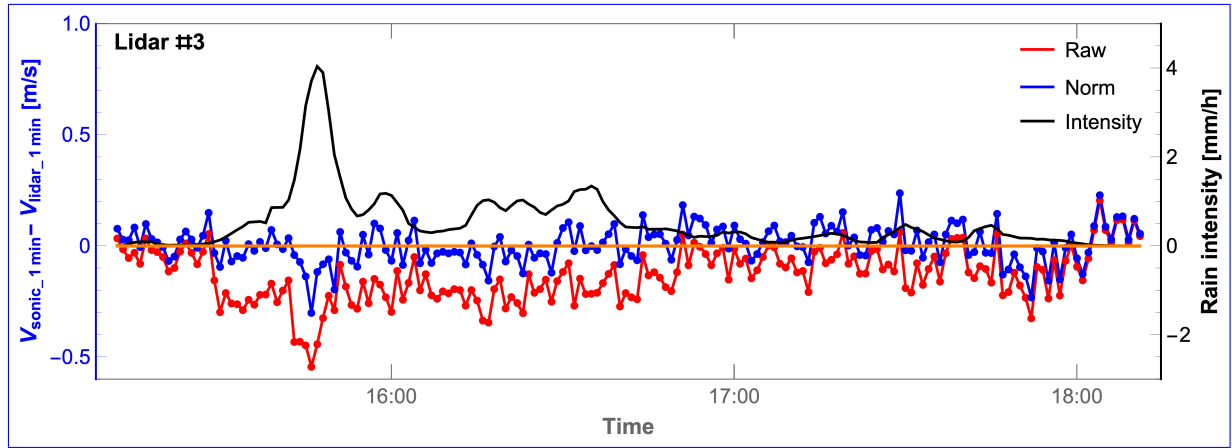
Figure 13. Difference of 1-minute averaged ~~radial~~ wind velocity between ~~the WindScanner lidars~~ lidar and ~~the~~ sonic ~~anemometer data measurements~~ together with the rain intensity (the solid black curve) from 15:12 to 18:11 ~~for lidar #1 ((a)~~UTC+1)~~and #3 (.~~ **(a)** Lidar #1 with the probe length of 1.2 m. **(b)** ~~)~~Lidar #3 with the probe length of 9.8 m. The raw and normalized lidar data ~~is~~ are marked in red ~~, while the blue curve~~ and ~~dots represent for the normalized lidar data~~blue.

series after normalization overlaps with that of the raw lidar data, especially when the rain intensity is below $0.2\ \mathrm{mmh}^{-1}$ after 17:00. For most of the three-hour comparison period, the wind velocity calculated by the raw lidar data is underestimated, as shown in Fig. 13b. This is because of the small projection of the raindrop velocity, which counteracts the aerosol projection and adversely affects the estimated wind velocity. As well, the red curve shows a radial velocity difference of over $0.5\ \mathrm{ms}^{-1}$.

In Fig. 14c, the 1-minute lidar wind velocity after the rain-suppressing normalization matches well with that of the sonic measurement for lidar #3 with a larger probe length, as the ~~filtered~~ normalized lidar data (blue dots) are in a closer agreement with the sonic measurements compared with the raw lidar data (red dots). For lidar #1 in Fig. 14a, there is no obvious improve-

ment after normalization by the spectral peak. However, the averaged bias in Fig. 14b and d demonstrate the performance of rain-suppressing normalization. It is clearly indicated by the red and blue fitted curves that the suppression becomes effective not only for lidar #3 when it rains, but also for lidar #1 with a short focus distance when the rain intensity ~~I_{rain}~~ is large. ~~We speculate that during light rain, the choice of~~ Due to the rare occurrence of raindrops passing through the laser beam with a condensed probe length, this method does not have a large impact on ~~the determined velocities of~~ velocity determinations by lidar #1 ~~due to the rare occurrence of raindrops passing through the laser beam with a very short probe length~~ during light rain, since at moderate rain there are only 0.05 raindrops remaining in the probe volume. These lead to the same conclusions discussed previously that rain-suppressing normalization performs well for the large probe length when it rains as well as for the small probe length when it rains more heavily than lightly.

6 Conclusions

~~By sampling the spectra of a Doppler lidar faster than the raindrop's beam transit time, the rain signal can be filtered away and the bias on the wind velocity estimation can be reduced~~ In this paper, we have shown an experimental proof-of-concept demonstration of a method to reduce the bias caused by precipitation on continuous-wave Doppler lidar measurements of wind speed. This is ~~verified by sampling lidar spectra~~ accomplished by sampling Doppler spectra faster than most raindrops' beam transit time, which in the current case was at 3 kHz ~~with different elevation angles and focus distances, and by comparing them with a reference sonic anemometer. In the method we propose,~~. Subsequently, the 3 kHz spectra are normalized with their peak values ~~before they are~~ to suppress strong backscatter signals from raindrops before being averaged down to 50 Hz from which the radial wind velocity is determined. ~~Over the whole range of rain intensities , we have observed a significant reduction of the bias of the lidar measurements relative to the sonic.~~

Results from lidar beams with different elevation angles and focus distances were studied under different rain intensities measured by a disdrometer. The derived wind velocities were compared with a sonic anemometer reference. From the comparison, we find that the rain-suppressing normalization has the most significant impact on reducing bias when the probe volume (growing with the fourth power of the focus distance) is the largest. However, when the probe volume is small (shorter focus distances), the impact of rain is limited. Rain-induced bias also varies according to elevation angle but to a lesser extent. However, the exact nature of these relations remains to be further verified and understood.

The tendency is that the more it rains, the ~~more the bias is reduced~~ stronger the bias and the more the rain-suppressing normalization is reducing the bias. For moderate rain intensity (we do not have a heavy rain period in our data), the range of the bias is reduced from the interval 0.1 to 0.4 ms^{-1} to 0.0 to 0.1 ms^{-1}.

The suggested method in this study could also be investigated for rain events (containing heavy rain) on several days and also for pulsed Doppler lidars even though their measurement volume is quite lar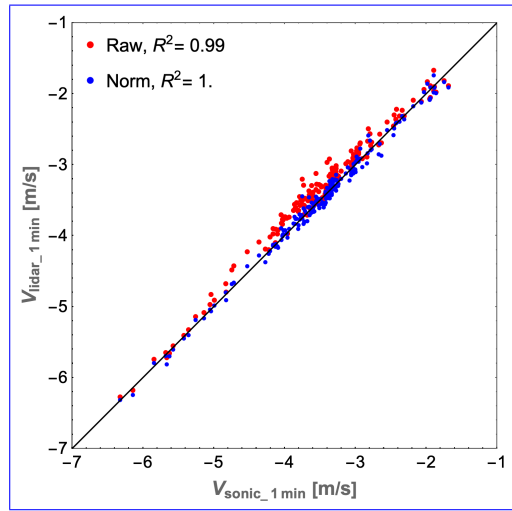ger than that of the continuous-wave lidars. Further investigations could also attempt to retrieve the falling velocity and the size distribution of raindrops using the fast Doppler spectra.
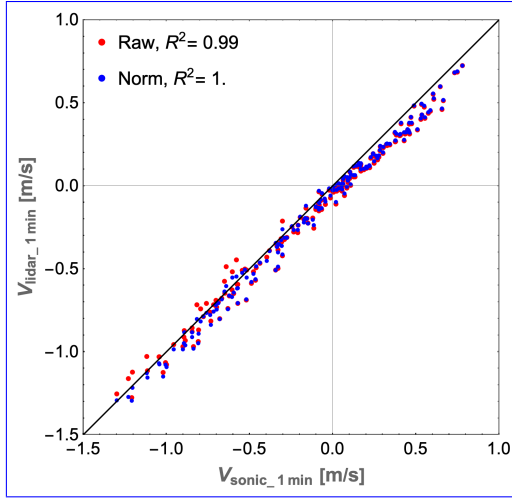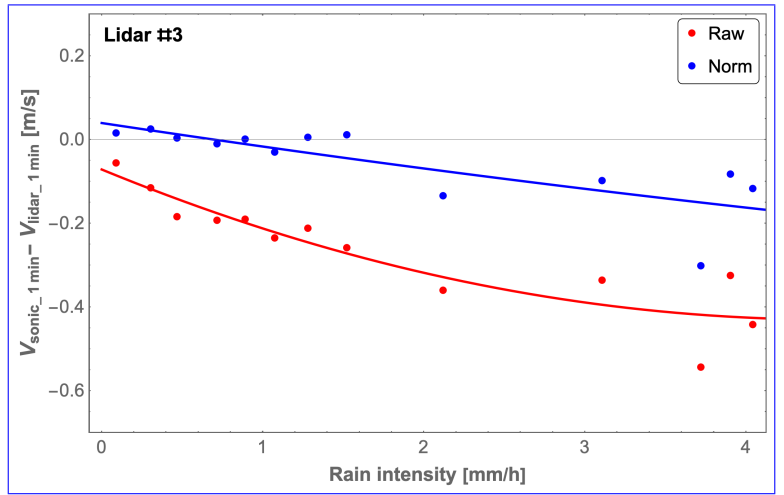
(a)
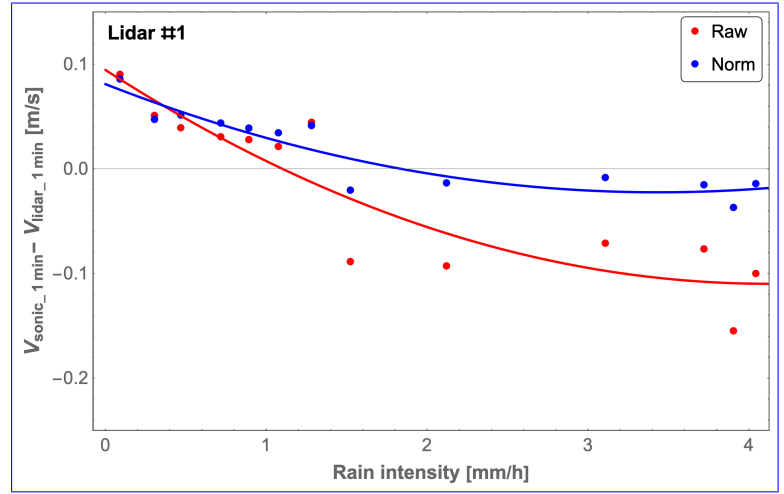
(b)

(c)

(d)

Figure 14. ~~The scatter plot of~~ 1-minute wind velocity ~~time series ((a), (c)) and the averaged bias~~ comparison between the lidar and sonic measurements ~~as a function of the rain intensity ((b), (d))~~ from 15:12 to 18:11 (UTC+1) for ~~WindScanner~~ lidar #1 (top row) and #3 (bottom row). ~~The red~~ (a) and ~~blue curves in~~ (c) Scatter plot of 1-minute wind velocity. (b) and (d) ~~represent the~~) Averaged bias and its fitted function as a function of the ~~bias~~ rain intensity. The raw and normalized lidar data are marked in red and blue.

References

Abari, C. F., Pedersen, A. T., and Mann, J.: An all-fiber image-reject homodyne coherent Doppler wind lidar, Optics express, 22, 25 880–25 894, 2014.

Angelou, N., Abari, F. F., Mann, J., Mikkelsen, T., and Sjöholm, M.: Challenges in noise removal from Doppler spectra acquired by a continuous-wave lidar, in: Proceedings of the 26th International Laser Radar Conference, Porto Heli, Greece, pp. 25–29, 2012a.

Angelou, N., Mann, J., Sjöholm, M., and Courtney, M.: Direct measurement of the spectral transfer function of a laser based anemometer, Review of scientific instruments, 83, 033 111, 2012b.

Angelou, N., Mann, J., and Dellwik, E.: Wind lidars reveal turbulence transport mechanism in the wake of a tree, Atmospheric Chemistry and Physics, 22, 2255–2268, 2022.

Angulo-Martínez, M., Beguería, S., Latorre, B., and Fernández-Raga, M.: Comparison of precipitation measurements by OTT Parsivel 2 and Thies LPM optical disdrometers, Hydrology and Earth System Sciences, 22, 2811–2837, 2018.

Aoki, M., Iwai, H., Nakagawa, K., Ishii, S., and Mizutani, K.: Measurements of rainfall velocity and raindrop size distribution using coherent Doppler lidar, Journal of Atmospheric and Oceanic Technology, 33, 1949–1966, 2016.

Bingöl, F., Mann, J., and Foussekis, D.: Conically scanning lidar error in complex terrain, Meteorologische Zeitschrift, pp. 189–195, 2009.

Bos, R., Giyanani, A., and Bierbooms, W.: Assessing the severity of wind gusts with lidar, Remote Sensing, 8, 758, 2016.

Bossanyi, E., Kumar, A., and Hugues-Salas, O.: Wind turbine control applications of turbine-mounted LIDAR, in: Journal of Physics: Conference Series, vol. 555, p. 012011, IOP Publishing, 2014.

Branlard, E., Pedersen, A. T., Mann, J., Angelou, N., Fischer, A., Mikkelsen, T., Harris, M., Slinger, C., and Montes, B.: Retrieving wind statistics from average spectrum of continuous-wave lidar, Atmospheric Measurement Techniques, 6, 1673–1683, 2013.

Brinkmeyer, E.: CW lidar for wind sensing featuring numerical range scanning and strong inherent suppression of disturbing reflections, in: Lidar Technologies, Techniques, and Measurements for Atmospheric Remote Sensing XI, vol. 9645, pp. 63–68, SPIE, 2015.

Cheynet, E., Jakobsen, J. B., Snæbjörnsson, J., Mikkelsen, T., Sjöholm, M., Mann, J., Hansen, P., Angelou, N., and Svardal, B.: Application of short-range dual-Doppler lidars to evaluate the coherence of turbulence, Experiments in Fluids, 57, 1–17, 2016.

Clima, T: Laser Precipitation Monitor Instruction for Use: 5.4110, https://www.thiesclima.com/db/dnl/5.4110.xx.x00_Laser_Precipitation_Monitor_eng.pdf, last access: 2 June 2023.

Davoust, S., Jehu, A., Bouillet, M., Bardon, M., Vercherin, B., Scholbrock, A., Fleming, P., and Wright, A.: Assessment and optimization of lidar measurement availability for wind turbine control, Tech. rep., National Renewable Energy Lab.(NREL), Golden, CO (United States), 2014.

Debnath, M., Iungo, G. V., Ashton, R., Brewer, W. A., Choukulkar, A., Delgado, R., Lundquist, J. K., Shaw, W. J., Wilczak, J. M., and Wolfe, D.: Vertical profiles of the 3-D wind velocity retrieved from multiple wind lidars performing triple range-height-indicator scans, Atmospheric Measurement Techniques, 10, 431–444, 2017.

Elshafei, B., Peña, A., Xu, D., Ren, J., Badger, J., Pimenta, F. M., Giddings, D., and Mao, X.: A hybrid solution for offshore wind resource assessment from limited onshore measurements, Applied Energy, 298, 117 245, 2021.

Glossary of Meteorology (June 2000): Rain, https://glossary.ametsoc.org/wiki/Rain, last access: 21 June 2023.

Gottschall, J., Papetta, A., Kassem, H., Meyer, P. J., Schrempf, L., Wetzel, C., and Becker, J.: Advancing Wind Resource Assessment in Complex Terrain with Scanning Lidar Measurements, Energies, 14, 3280, 2021.

Guo, F., Mann, J., Peña, A., Schlipf, D., and Cheng, P. W.: The space-time structure of turbulence for lidar-assisted wind turbine control, Renewable Energy, 2022.

Held, D. P. and Mann, J.: Comparison of methods to derive radial wind speed from a continuous-wave coherent lidar Doppler spectrum, Atmospheric Measurement Techniques, 11, 6339–6350, 2018.

Henderson, S. W., Hale, C. P., Magee, J. R., Kavaya, M. J., and Huffaker, A. V.: Eye-safe coherent laser radar system at 2.1 μm using Tm, Ho: YAG lasers, Optics letters, 16, 773–775, 1991.

Izumi, Y. and Barad, M. L.: Wind speeds as measured by cup and sonic anemometers and influenced by tower structure, Journal of Applied Meteorology and Climatology, 9, 851–856, 1970.

Jena, D. and Rajendran, S.: A review of estimation of effective wind speed based control of wind turbines, Renewable and Sustainable Energy Reviews, 43, 1046–1062, 2015.

Jin, L., Angelou, N., Mann, J., and Larsen, G. C.: Improved wind speed estimation and rain quantification with continuous-wave wind lidar, in: Journal of Physics: Conference Series, vol. 2265, p. 022093, IOP Publishing, 2022.

Leica Geosystems: Introduction of Leica Total Station, https://leica-geosystems.com/products/total-stations, last access: 12 March 2023.

Li, J., Wang, X., and Yu, X. B.: Use of spatio-temporal calibrated wind shear model to improve accuracy of wind resource assessment, Applied energy, 213, 469–485, 2018.

Mann, J., Angelou, N., Arnqvist, J., Callies, D., Cantero, E., Arroyo, R. C., Courtney, M., Cuxart, J., Dellwik, E., Gottschall, J., et al.: Complex terrain experiments in the new european wind atlas, Philosophical Transactions of the Royal Society A: Mathematical, Physical and Engineering Sciences, 375, 20160 101, 2017.

Menke, R., Vasiljević, N., Wagner, J., Oncley, S. P., and Mann, J.: Multi-lidar wind resource mapping in complex terrain, Wind Energy Science, 5, 1059–1073, 2020.

Mikkelsen, T., Mann, J., Courtney, M., and Sjöholm, M.: Windscanner: 3-D wind and turbulence measurements from three steerable Doppler lidars, in: IOP conference series: earth and environmental science, vol. 1, p. 012018, IOP Publishing, 2008.

Mikkelsen, T., Angelou, N., Hansen, K., Sjöholm, M., Harris, M., Slinger, C., Hadley, P., Scullion, R., Ellis, G., and Vives, G.: A spinner-integrated wind lidar for enhanced wind turbine control, Wind Energy, 16, 625–643, 2013.

Mikkelsen, T., Sjöholm, M., Angelou, N., and Mann, J.: 3D WindScanner lidar measurements of wind and turbulence around wind turbines, buildings and bridges, in: IOP Conference Series: Materials Science and Engineering, vol. 276, p. 012004, IOP Publishing, 2017.

Mikkelsen, T., Sjöholm, M., Astrup, P., Peña, A., Larsen, G., Van Dooren, M., and Sekar, A. K.: Lidar Scanning of Induction Zone Wind Fields over Sloping Terrain, in: Journal of Physics: Conference Series, vol. 1452, p. 012081, IOP Publishing, 2020.

Peña, A., Hasager, C. B., Gryning, S.-E., Courtney, M., Antoniou, I., and Mikkelsen, T.: Offshore wind profiling using light detection and ranging measurements, Wind Energy: An International Journal for Progress and Applications in Wind Power Conversion Technology, 12, 105–124, 2009.

Peña, A., Hasager, C., Badger, M., Barthelmie, R., Bingöl, F., Cariou, J.-P., Emeis, S., Frandsen, S., Harris, M., Karagali, I., Larsen, S., Mann, J., Mikkelsen, T., Pitter, M., Pryor, S., Sathe, A., Schlipf, D., Slinger, C., and Wagner, R.: Remote Sensing for Wind Energy, no. 0084(EN) in DTU Wind Energy E, DTU Wind Energy, Denmark, 2015.

Press, W. H., Vetterling, W. T., Teukolsky, S. A., and Flannery, B. P.: Numerical recipes, Citeseer, 1988.

Samadianfard, S., Hashemi, S., Kargar, K., Izadyar, M., Mostafaeipour, A., Mosavi, A., Nabipour, N., and Shamshirband, S.: Wind speed prediction using a hybrid model of the multi-layer perceptron and whale optimization algorithm, Energy Reports, 6, 1147–1159, 2020.

Sathe, A. and Mann, J.: A review of turbulence measurements using ground-based wind lidars, Atmospheric Measurement Techniques, 6, 3147–3167, 2013.

Schlipf, D., Haizmann, F., Cosack, N., Siebers, T., and Cheng, P. W.: Detection of wind evolution and lidar trajectory optimization for lidar-assisted wind turbine control, 2015.

Sempreviva, A. M., Barthelmie, R. J., and Pryor, S.: Review of methodologies for offshore wind resource assessment in European seas, Surveys in Geophysics, 29, 471–497, 2008.

Sjöholm, M., Angelou, N., Hansen, P., Hansen, K. H., Mikkelsen, T., Haga, S., Silgjerd, J. A., and Starsmore, N.: Two-dimensional rotor-craft downwash flow field measurements by lidar-based wind scanners with agile beam steering, Journal of Atmospheric and Oceanic Technology, 31, 930–937, 2014.

Tilg, A.-M., Hasager, C., Veien, F., Badger, M., Rasmussen, M., Verhoef, J., and Skrzypinski, W.: Precipitation in the context of wind turbine blade erosion, 2020.

Träumner, K., Handwerker, J., Wieser, A., and Grenzhäuser, J.: A synergy approach to estimate properties of raindrop size distributions using a Doppler lidar and cloud radar, Journal of Atmospheric and Oceanic Technology, 27, 1095–1100, 2010.

Türk, M. and Emeis, S.: The dependence of offshore turbulence intensity on wind speed, Journal of Wind Engineering and Industrial Aerodynamics, 98, 466–471, 2010.

Van Ulden, A. and Holtslag, A.: Estimation of atmospheric boundary layer parameters for diffusion applications, Journal of Applied Meteorology and Climatology, 24, 1196–1207, 1985.

Vasiljević, N., LM Palma, J. M., Angelou, N., Carlos Matos, J., Menke, R., Lea, G., Mann, J., Courtney, M., Frölen Ribeiro, L., and MGC Gomes, V. M.: Perdigão 2015: methodology for atmospheric multi-Doppler lidar experiments, Atmospheric Measurement Techniques, 10, 3463–3483, 2017.

Viselli, A., Filippelli, M., Pettigrew, N., Dagher, H., and Faessler, N.: Validation of the first LiDAR wind resource assessment buoy system offshore the Northeast United States, Wind Energy, 22, 1548–1562, 2019.

Wei, T., Xia, H., Hu, J., Wang, C., Shangguan, M., Wang, L., Jia, M., and Dou, X.: Simultaneous wind and rainfall detection by power spectrum analysis using a VAD scanning coherent Doppler lidar, Optics express, 27, 31 235–31 245, 2019.

Wei, T., Xia, H., Yue, B., Wu, Y., and Liu, Q.: Remote sensing of raindrop size distribution using the coherent Doppler lidar, Optics Express, 29, 17 246–17 257, 2021.

Wildmann, N., Päschke, E., Roiger, A., and Mallaun, C.: Towards improved turbulence estimation with Doppler wind lidar velocity-azimuth display (VAD) scans, Atmospheric Measurement Techniques, 13, 4141–4158, 2020.

Zhang, L. and Yang, Q.: A method for yaw error alignment of wind turbine based on LiDAR, IEEE Access, 8, 25 052–25 059, 2020.